



## Direct microencapsulation of Ionic-Liquid-Based shear thickening fluid via rheological behavior transition for functional applications

Shusheng Chen<sup>a,b,c</sup>, Ying Zhao<sup>a</sup>, Heng Zhang<sup>a</sup>, Peidong Xu<sup>d</sup>, Zhenyu Jiang<sup>d</sup>, He Zhang<sup>e,\*</sup>, Jinglei Yang<sup>a,f,g,\*</sup>

<sup>a</sup> Department of Mechanical and Aerospace Engineering, The Hong Kong University of Science and Technology, Clear Water Bay, Hong Kong SAR, China

<sup>b</sup> Guangdong Provincial Key Laboratory of Functional Substances in Medicinal Edible Resources and Healthcare Products, School of Chemistry and Environmental Engineering, Hanshan Normal University, Chaozhou, Guangdong 521041, China

<sup>c</sup> State Key Laboratory of Molecular Engineering of Polymers, Department of Macromolecular Science, Fudan University, Shanghai 200433, China

<sup>d</sup> School of Civil Engineering and Transportation, State Key Laboratory of Subtropical Building Science, South China University of Technology, Guangzhou 510640, China

<sup>e</sup> National Engineering Research Center of Novel Equipment for Polymer Processing, Key Laboratory of Polymer Processing Engineering (SCUT), Ministry of Education, South China University of Technology, Guangzhou 510641, China

<sup>f</sup> HKUST Shenzhen-Hong Kong Collaborative Innovation Research Institute, Futian, Shenzhen 518048, China

<sup>g</sup> Foshan SMN Materials Tech Co., Ltd., Nanhui District, Foshan 528200, China



### ARTICLE INFO

#### Keywords:

Shear thickening fluid (STF)  
Ionic liquid  
Microencapsulation  
Rheological behavior transition  
Impact resistance  
Conductivity restoration

### ABSTRACT

In nature, various stimuli-responsive materials, such as bone, are self-adaptable to external loading by modulating their mechanical properties to prevent failure and self-healing after damage. Herein, for the first time, an oil-in-oil solvent-evaporation approach is proposed to directly microencapsulate a multifunctional self-adaptive material—ionic-liquid-based shear thickening fluid (ILSTF)—via rheological behavior transition. As the co-solvent completely changed the rheological responses of the dispersed phase, this approach proved ideal for encapsulating STFs with high viscosity and shear-thickening behavior. The resultant ILSTF microcapsules (MCs) exhibited high thermal stability (initial decomposition temperature of ~380 °C) and controllable size at the micrometer level from 66 to 260 μm. The typical ILSTF MCs were incorporated into an elastomer matrix, achieving 33 % and 67 % enhancement of energy absorption ability compared with the pure polymer and IL MCs-embedded composites, respectively. Furthermore, the circuit comprised of ILSTF MCs-incorporated flexible conductor exhibited not only electrical stability upon impact, but also autonomic conductivity restoration after injury, demonstrating that the ILSTF MCs can serve as a multifunctional agent for emerging applications, such as deformable circuits and battery safety.

### 1. Introduction

Materials with switchable and field-responsive mechanical properties, such as bone [1] and fish scales [2], are widespread in nature and endow many species with traits crucial for survival. The triggers for these self-adaptive materials can be humidity, pH, temperature, stress, damage, and so on [3]. Inspired by nature, diversified synthetic autonomous/adaptive materials were explored to mimic the natural materials functionally/structurally [4–8]. Shear thickening fluid (STF), a non-Newtonian liquid, is one of the self-adaptable biomaterials that exhibit an abrupt increase in viscosity once the shear rate passes its critical shear rate and returns to the initial state when the shear stress is removed. This

reversible transition from a low to a high viscosity state is associated with a significant energy absorption that can be harnessed for impact protection [9–11]. The traditional STF is concentrated colloidal suspensions of dispersing particles in an aqueous or organic carrier medium, including water, ethylene glycol, and low molecular weight polyethylene glycol. However, volatilization of these carrier liquids and easy precipitation of particles in the dispersing medium weaken the defensive performances of STF and STF-treated composites [12].

Recently, a few studies reported that certain colloidal particles can be suspended stably in room-temperature ionic liquids (ILs) and showed shear-thickening behavior [13–15]. ILs are composed entirely of ions. They have received considerable interest in many research fields

\* Corresponding authors at: Department of Mechanical and Aerospace Engineering, The Hong Kong University of Science and Technology, Clear Water Bay, Hong Kong SAR, China.

E-mail addresses: [zhanghe@scut.edu.cn](mailto:zhanghe@scut.edu.cn) (H. Zhang), [maeyang@ust.hk](mailto:maeyang@ust.hk) (J. Yang).

because of their novel physicochemical properties, such as super thermal and chemical stabilities, high conductivity, and wide electrochemical potential window. From the viewpoint of carrier media for colloidal particles, IL-based STFs (ILSTFs) are not only able to serve as energy absorption agents due to their shear-thickening performance, but they are also of great interest in terms of their electrochemical applications [16,17]. However, as STF is a liquid with high viscosity and strong hygroscopicity, it is difficult to be integrated into other matrices and easily deteriorates during usage, compromising its superiority in practical application.

A few investigations have been attempted to solve or partially solve these challenges. For fabrics impregnated with STF, Wagner et al. [18–20] tried to package and seal the whole fabrics within the polyethylene film to reduce the external influence. To incorporate and reserve STF in the composites, polymer foams [21] and dampers [22] have been adopted to carry STF for anti-impact and damping applications. In the patented works, hollow tubular or fiber structures by co-extruding [23] or coaxial electrospinning [24] have also been proposed to enclose STF as liquid cores. Although these approaches minimize the negative effect of external surroundings, reprocessing these packages of STF into various matrices is challenging. Recently, Zhang et al. [25,26] reported the encapsulation of STF liquid core in double-walled capsules via a syringe instilling process and interfacial polymerization. Liu et al. [27,28] proposed an orifice coagulation batch method to encapsulate STF with a pomelo-like hierarchical structure using an instilling process. Compared with the previous isolating methods, encapsulation is the most promising technique, not only because it can isolate the STF within capsules to minimize the influence from the surrounding environment, but it can also solidify the STF for easy handling and integration into matrices. However, it is a significant challenge to encapsulate STF due to its high viscosity and multiple ingredients. In particular, emulsification under shear force by either the microfluidic method or bulk agitation is an indispensable part of the encapsulation, but the shear-thickening effect of STF makes it extraordinarily difficult to be emulsified directly. The viscosity of STF increases notably under a high shear force that generally results in large-size emulsion droplets. Until now, only fluidic emulsion by pumped syringe dropping system has been applied for STF encapsulation. Moreover, these reports can only prepare STF capsules at the millimeter level [25–28], which limits their applications. Apart from the difficulty in controlling the size of capsules, the low efficiency in emulsion production of the syringe stilling process makes it unsuitable for scalable applications.

In the present work, we aim to develop a direct and scalable microencapsulation method for ILSTF. The oil-in-oil (o/o) emulsion solvent evaporation approach will be utilized owing to its unique microencapsulation mechanism and advantages [29]: 1) The dilution of co-solvent can significantly decrease the viscosity of the dispersed phase and eliminate its shear-thickening behavior before microencapsulation, which makes it suitable for emulsification via mechanical stirring; 2) The core can transfer back to shear-thickening property with the evaporation of co-solvent and phase separation of the shell-forming polymer; 3) The diameter of the resulting ILSTF capsules can be controlled at the micrometer level by the agitation rate. The incorporation of such ILSTF microcapsules (MCs) into flexible conductors could provide the corresponding circuits with electrical stability upon impact and autonomous conductivity restoration after damage.

## 2. Results and discussion

### 2.1. Rheological properties of ILSTF

The IL carrier liquid used in our work was 1-butyl-methylimidazolium tetrafluoroborate ([Bmim][BF<sub>4</sub>]). The dispersions of fumed silica Aerosil 200 with different weight percentages (6, 8, 10, 12, and 14 wt%) in IL were prepared and denoted as ILSTF6, ILSTF8, ILSTF10, ILSTF12,

and ILSTF14. As shown in Fig. 1a, the viscosities of ILSTFs are sensitive to shear rate, which maintains relatively low values at low shear rates, but increases significantly at higher shear rates. The shear-thickening performance of ILSTFs is ascribed to the solvation layers of dispersing silica [14] and improved with increasing silica concentration, which is in good agreement with the results of previous investigations [13,30]. Fig. 1b shows the quasi-static viscosities of ILSTFs that are defined as the average viscosity under a low shear rate of 0.1 s<sup>-1</sup> for 1 min. Although the high silica concentration of ILSTFs enhances the shear-thickening effect, it results in higher quasi-static viscosity. As presented in Fig. 1c and S1, ILSTF6, ILSTF8, and ILSTF10 start flowing immediately when the vial is laid flat, indicating their good flowing behaviors compared with the poor fluidity of ILSTF12 and ILSTF14. To strike a balance between shear-thickening performance and apparent fluidity, ILSTF10 was chosen as a typical sample for the following study.

The influence of the addition of acetone on the rheological response of ILSTF was further investigated before the microencapsulation study, and the result is given in Fig. 1d. The shear-thickening effect of ILSTF10 reduces with the increase of the acetone ratio. No shear-thickening response is observed when the weight ratios of ILSTF10 to acetone are 10:1 and 1:10. This implies that the addition of a suitable amount of acetone completely changes the shear response of ILSTF, which provides an essential guideline for microencapsulation. Fig. 1e illustrates the mechanism of rheological behaviors regarding silica dispersion in IL with/without acetone according to the previous reports [13,14]. For the dispersion of silica in pure IL, silica nanoparticles aggregate and form clusters because of hydrodynamic force under a high shear rate [31], activating the shear-thickening response. In contrast, the increase in shear rate hardly leads to hydro-cluster formation due to the large interparticle distances for the dispersion diluted with acetone [32]. Therefore, a non-aqueous emulsion containing ILSTF as dispersed phase should be more easily achieved with the assistance of acetone.

It is worth noting that the shear thickening of ILSTFs performs better than the traditional STFs composed of polyethylene glycol MW 200 (PEG200) (Fig. 1a and S2). In addition, the critical shear rate for shear-thickening onset and the ratio of maximum viscosity to the viscosity in the critical shear rate (shear-thickening ratio) are used as the two parameters to evaluate the performance of STFs comprising different liquid carriers [12]. As shown in Fig. 1f, the shear-thickening ratio of ILSTF10 is around 35, while the dispersions of 10 wt% fumed silica in several other carrier media [33,34], including ethylene glycol, propylene glycol, polyethylene glycol, and polypropylene glycols with different molecular weights, display weak shear-thickening responses with the shear-thickening ratios lower than 8. A critical shear rate of 2.5 s<sup>-1</sup> for ILSTF10 is obtained, which is lower than those of other STFs. Although the shear-thickening effect of ILSTF10 decreases with the addition of acetone, the mixture of ILSTF10 and acetone with a ratio of 100:1 displays satisfying shear-thickening performance with the shear-thickening ratio of 26 and the critical shear rate of 3.2 s<sup>-1</sup>, respectively. This indicates that the shear-thickening properties of ILSTF will not be very sensitive to the residual acetone that may remain in the ILSTF MCs after the microencapsulation process using acetone as the diluent.

### 2.2. Preparation and characterization of ILSTF MCs

Fig. 2a illustrates the mechanism for the ILSTF microencapsulation with acrylonitrile–butadienestyrene copolymer (ABS) shell via an o/o emulsion solvent evaporation method (see Supplementary Material for experimental details). The dispersed phase consisted of a diluted dispersion of silica in the acetone solution of ABS and IL. After adding the dispersed phase into the paraffin oil under mechanical stirring, an o/o emulsion was produced and became stable after agitation for 30 min. With the gradual evaporation of acetone at room temperature (~25 °C), the ABS separated from the emulsion droplets to form a solid shell surrounding the liquid core. When the acetone and ABS were removed completely, only the silica dispersion in IL remained in the liquid core of

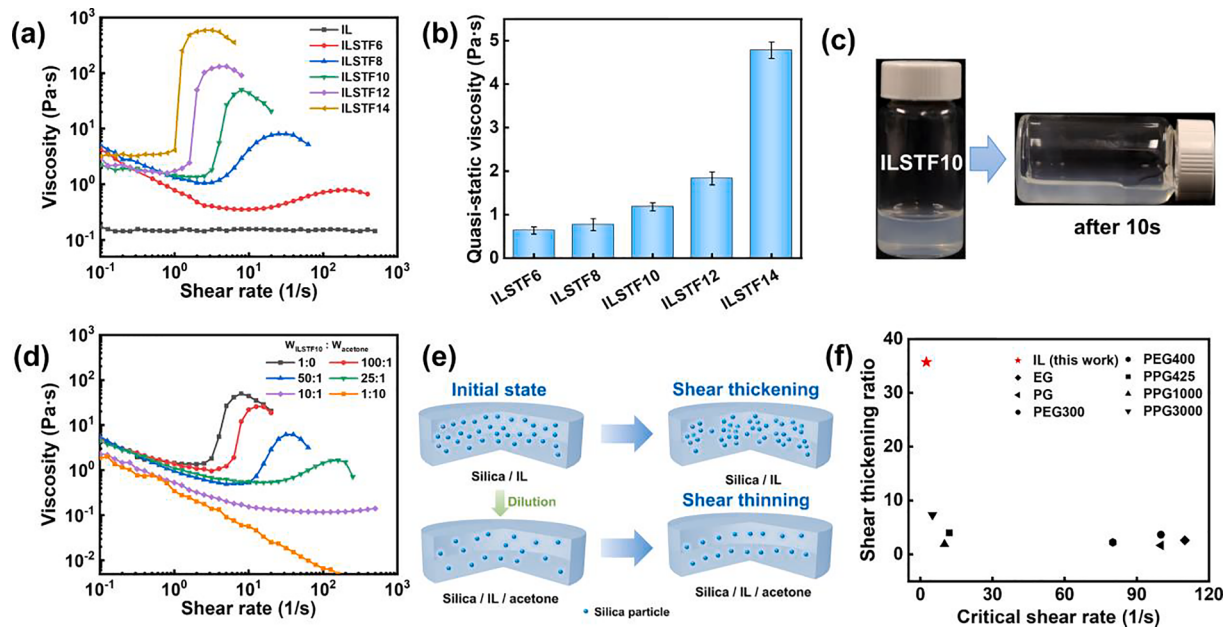


**Fig. 1.** (a) Viscosity as a function of shear rate for pure IL and ILSTFs. (b) Quasi-static viscosity of ILSTFs. (c) Photographic demonstration of the macroscopic fluidity of ILSTF10. (d) Viscosity as a function of shear rate for ILSTF10 diluted with acetone. (e) Schematic illustration of microstructure transition under shearing for the dispersion of silica in IL with/without acetone. (f) The comparison of shear thickening ratio and critical shear rate about the dispersions of 10 wt% Aerosil 200 silica in different carrier media, including 1-butyl-methylimidazolium tetrafluoroborate (IL), ethylene glycol (EG), propylene glycol (PG), polyethylene glycol with molecular weights of 300 and 400 g/mol (PEG300 and PEG400), and polypropylene glycol with molecular weights of 425, 1000, and 3000 g/mol (PPG425, PPG1000, and PPG3000), respectively [33,34].

MCs, namely ILSTF MCs. The primary reason for choosing ABS as a shell-forming ingredient is that ABS copolymer is composed of polar and nonpolar groups. The nitrile polar groups of ABS display strong interaction with acetone, while the other nonpolar hydrocarbon groups exhibit an affinity with paraffin oil. Therefore, after phase separation, the ABS copolymer chain can be adsorbed at the droplet/paraffin interfaces to improve the emulsion stability [35]. Several other acetone-soluble polymers, such as polystyrene (PS), poly(methyl methacrylate) (PMMA), and poly(lactic acid) (PLA), were evaluated as potential shell materials, but all failed to achieve stable emulsions and final MCs.

Before microencapsulation, a ternary phase diagram of ABS-IL-acetone is constructed to provide information about the phase boundary that demarcates the homogeneous and separated phases (Fig. 2b). In our study, the composition of the mixture in the two-phase region (black triangle spot, the IL-to-acetone mass ratio is 6:1) fails to achieve emulsion due to the phase separation of the dispersed phase. When the mass ratio of IL to acetone is 1:2 (black triangle spot), a homogeneous dispersed mixture can be obtained but fails to prepare MCs because of the high volatility of acetone and the too fast phase separation. According to the mechanism of solvent-evaporation microencapsulation, in the shell-forming process of microencapsulation, a sufficient amount of co-solvent is beneficial for polymer swelling, migration, and rearrangement, which finally achieves robust polymer shells on the o/o droplet interfaces. Therefore, the IL-to-acetone mass ratio of 1:10 (green circle spots) is used to prepare MCs in this work. Notably, this weight percentage of acetone also eliminates the shear-thickening behavior of ILSTF based on the above discussion (Fig. 1d).

After stirring for 0.5 h, the emulsion was taken and observed by microscope. Fig. 2c shows the diameter reduces from  $383 \pm 65 \mu\text{m}$  of the droplets to  $251 \pm 45 \mu\text{m}$  of the MCs, implying the evaporation of acetone. The gradual transition from translucent droplets to opaque MCs indicates the phase separation and shell formation by ABS for the MCs. Dyed liquid (Rhodamine 6G in the core) is released after compressing a few MCs between two glass slides, which preliminarily validates the successful loading of the silica dispersion in IL (Fig. 2d). SEM image (Fig. 2e) displays that ILSTF MCs are nearly spherical with uneven

surfaces. The wrinkles on the MC surface are caused by shrinking with the loss of acetone [36]. Several MCs were ruptured by a razor blade and washed with ethanol before SEM imaging. A ruptured ILSTF MC comprised of a core-shell structure is observed in Fig. 2f. A few ILSTF MCs were extracted by ethanol to remove IL and then ruptured manually, followed by EDS characterization. As can be seen from Fig. 2g, the remaining core of ruptured MC is silica, indicating that the core of MC contains silica dispersion.

The composition of the fabricated MCs was further examined by FTIR. As given in Fig. 2h, in contrast to the spectrum of ILSTF, ILSTF MCs exhibit a new band at  $2338 \text{ cm}^{-1}$  related to the acrylonitrile unit  $\text{—C}\equiv\text{N}$  of ABS, which is distinguished clearly from the enlarged spectra shown in Fig. S3b, suggesting that the ILSTF is successfully encapsulated with ABS shell. The absorption at  $1710 \text{ cm}^{-1}$  attributed to the  $\text{—C=O}$  group of acetone (Fig. S3a) cannot be observed in the spectrum of ILSTF MCs, which indicates the complete evaporation of acetone during the microencapsulation process. The TGA result of ILSTF MCs exhibits that the initial decomposition temperature of ILSTF MCs is around  $380^\circ\text{C}$  (Fig. 2i). Their weight losses at  $150$ ,  $200$ ,  $250$ , and  $300^\circ\text{C}$  for 1 h are only  $0.8$ ,  $2.1$ ,  $4.2$ , and  $12.5$  wt%, respectively, indicating their super high thermal stability (Fig. 2j). The excellent thermal stability of ILSTF MCs results from both the thermally stable ILSTF core and ABS shell (Fig. S4), which performs better than the traditional STFs encapsulated with PU shell [25] or calcium alginate shell [28].

### 2.3. Parametric investigation for optimal microencapsulation of ILSTF MC

In terms of solvent-evaporation microencapsulation, the ratio of core to shell plays a vital role in the properties of resultant MCs [36,37]. Fig. 3a–c show the general appearance, outer surface, and cross-sections of the obtained MCs using the core-to-shell ratio of 2:1, 4:1, and 6:1, respectively. Although core-shell MCs can be obtained for all these ratios, their morphologies exhibit apparent differences. When the  $M_{\text{ILSTF}}:M_{\text{ABS}}$  ratio is 2:1, the MC shells seriously buckle and shrink with nano-sized pores distributed on the outer surface. The cross-section of the

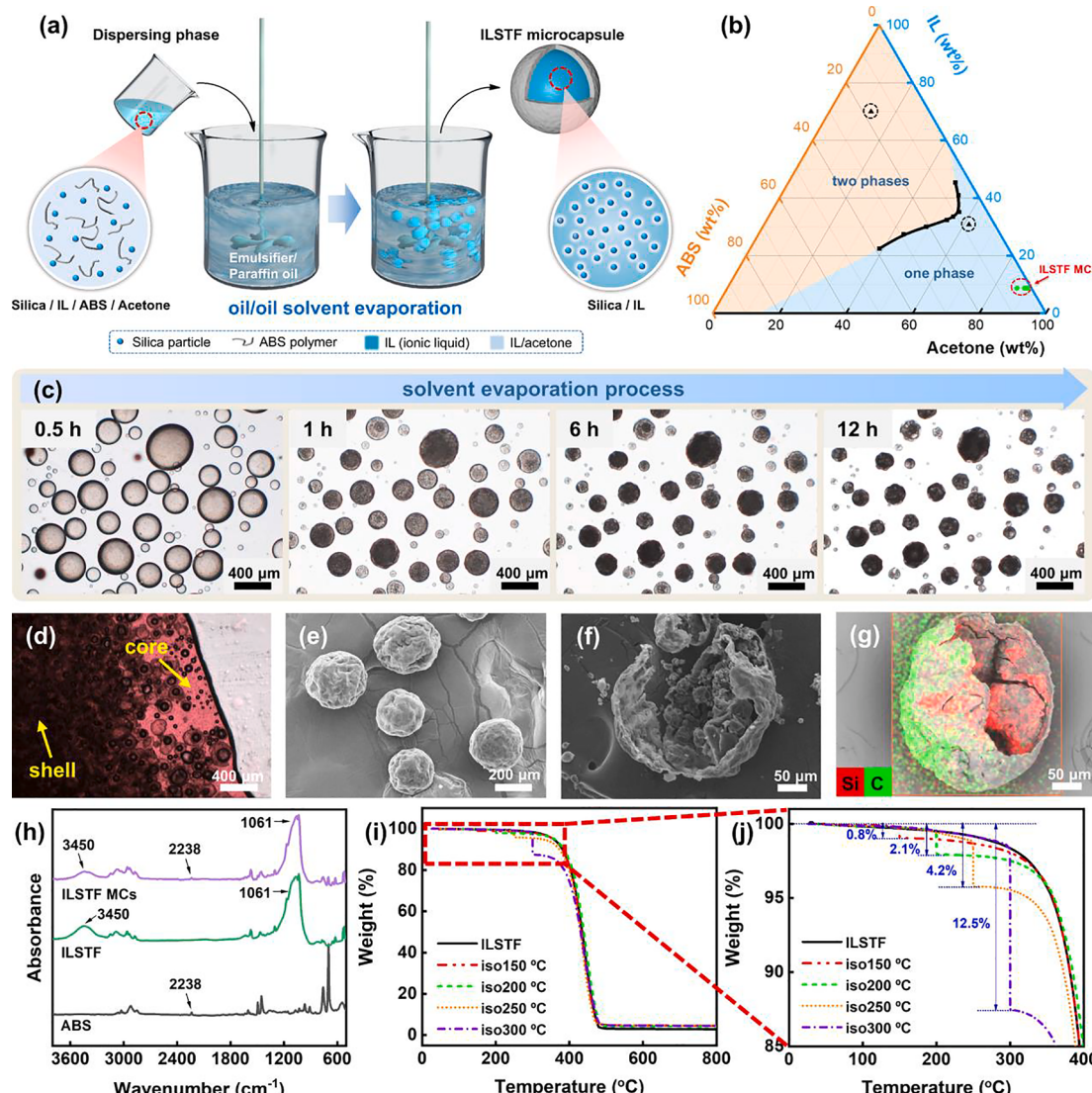


**Fig. 2.** (a) Schematic illustration of ILSTF microencapsulation via an *o/o* emulsion solvent evaporation method. (b) Ternary phase diagram of ABS-acetone-IL. The compositions of dispersed phase failed to prepare ILSTF MCs are shown by black triangle spots in the black frame. The compositions of dispersed phase used to prepare ILSTF MCs are shown by green circle spots in the red frame. (c) Optical microscopy images of *o/o* droplets that were collected after emulsification for 0.5 h and monitored during the solvent evaporation process. (d) Optical microscopy image of crushing ILSTF MCs. SEM images of (e) intact ILSTF MCs and (f) a ruptured ILSTF MC. (g) SEM-EDS mapping image of a ruptured ILSTF MC. (h) FTIR spectra of ILSTF MCs, ILSTF, and ABS. (i) TGA thermal and isothermal curves of ILSTF MCs. For the condition of isothermal curves, the samples were first heated to 150, 200, 250, and 300 °C, respectively, and then kept isothermal for 1 h before they were finally heated to 800 °C. (j) The enlarged TGA curves of decomposition areas in the red frame. (For interpretation of the references to colour in this figure legend, the reader is referred to the web version of this article.)

shell indicates it is porous, containing lots of vesicles at several microns. The thickness of the shell, measured from the cross-sectional view image, is about 10 μm. When increasing the ratio of ILSTF to ABS, the wrinkle of the shell reduces, and the outer surface becomes smooth. The tiny pores can hardly be observed on the exterior surfaces or the cross-section of the shell. The shell thickness decreases to around 5 μm and 2 μm for the core-to-shell weight ratio of 4:1 and 6:1, respectively. The morphology difference is caused by the phase separation rate of the polymer in the dispersed phase. For a higher mass ratio of the shell, the phase separation of the polymer is easier. The polymer shell separates and covers the droplets at the early stage of solvent evaporation. As more solvent is removed, the droplets with thin shells shrank further, which forces the shell to buckle. In the meantime, solvent evaporation through the thicker shells of MC results in larger pores, which produces MCs with more porous shells [36]. The ILSTF MCs with a core-to-shell ratio of 8:1 are prepared, but they are not strong enough and thus collapse under a high vacuum during SEM imaging (Fig. S5). To

investigate the effect of phase separation rate on the MC morphologies, solvent evaporation at the heating state was conducted. Fig. S6 shows that ILSTF MCs (core-to-shell ratio of 4:1) have a lumpy shape that may be caused by the bubbling away of acetone at 40 °C, while the “brain-skin” morphology is observed due to the extreme evaporation rate of acetone at 60 °C. The shells of these two MCs are porous and composed of plenty of micro-sized pores, which is in line with the above discussion of the shell-forming process. Therefore, in our study, the MC microencapsulation is in a thermodynamic equilibrium state. A slower solvent evaporation rate is beneficial for the uniform migration of the polymer from the dispersed phase to the interface, forming a denser core–shell structure with better barrier performance [38].

Fig. 3d shows the core fraction of ILSTF MCs with different core-to-shell ratios measured by UV-vis spectroscopy. The characteristic absorption peak of ILSTF is at 211 nm in the UV-vis spectrum (Fig. S7a), corresponding to the absorption of IL ([Bmim][BF<sub>4</sub>]) [39]. A linear equation ( $Y = 0.016X + 0.059$ ,  $R^2 = 0.99856$ ) is fitted from the

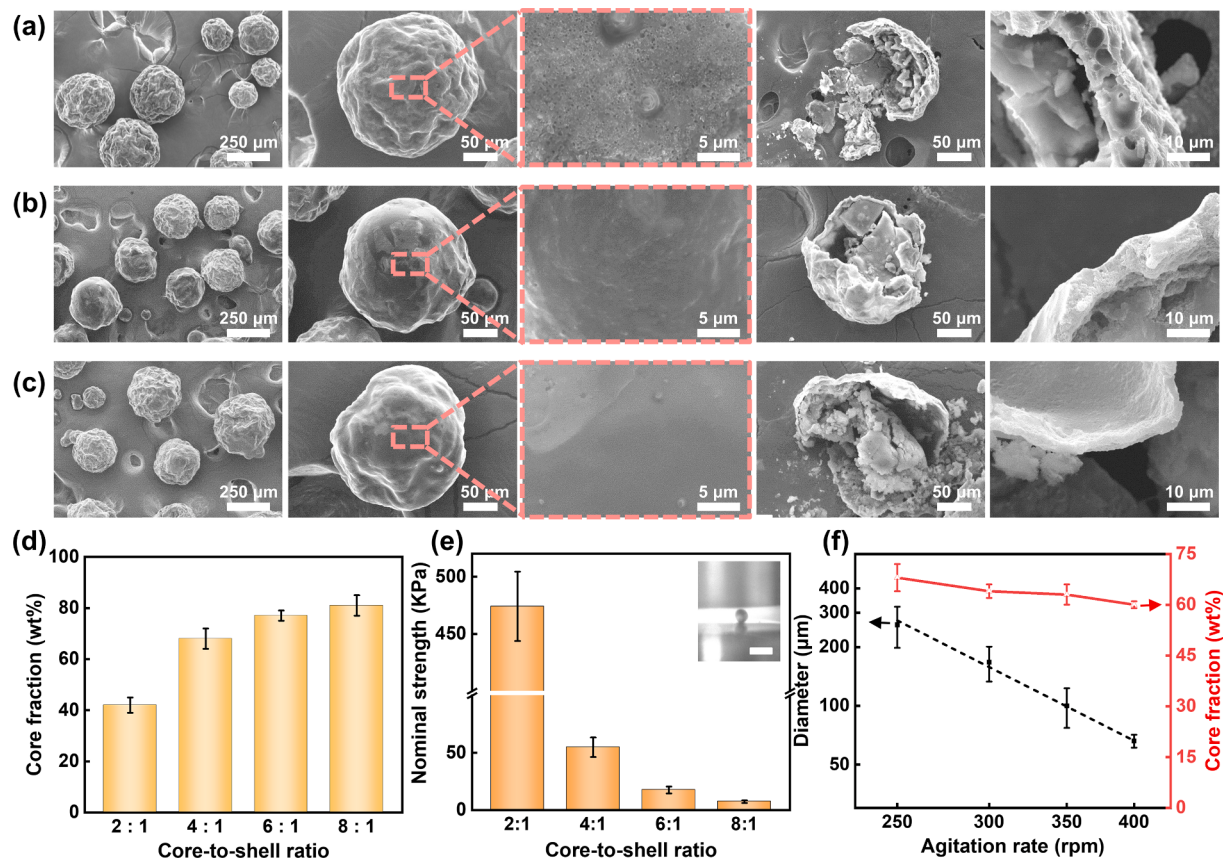


**Fig. 3.** SEM images of ILSTF MCs prepared with core-to-shell mass ratios of (a) 2:1, (b) 4:1, and (c) 6:1. (d) Core fraction and (e) nominal strength of ILSTF MCs as a function of core-to-shell mass ratio. The insert is the photo of a single MC under quasi-static compression. The white scale bar indicates 500 μm in the inset. (f) Diameter and core fraction of ILSTF MCs with a core-to-shell mass ratio of 4:1 as a function of agitation rate.

relationship between the concentrations of ILSTF aqueous solutions (ranging from 0 to 150 mg/L) and their corresponding absorbance (Fig. S7b). By utilizing this equation, the core fraction of ILSTF MCs can be quantified from a certain weight percentage of ruptured MCs in water. The core fractions of ILSTF MCs are 42 ± 3, 68 ± 5, 77 ± 2, 81 ± 4 wt% for the core-to-shell ratio of 2:1, 4:1, 6:1, and 8:1, respectively, indicating that the core fraction of ILSTF MCs increases when reducing the weight ratio of the shell.

The effect of the core-to-shell ratio on the mechanical properties of ILSTF MCs was further investigated by quasi-static compression. The typical nominal stress-strain curves of ILSTF MCs with different  $M_{\text{ILSTF}}:M_{\text{ABS}}$  ratios are presented in Fig. S8. The nominal strength decreases steeply with an increase of the core-to-shell ratio, namely from 474 ± 30 to 7 ± 1 KPa for the ratio of 2:1 and 8:1, respectively (Fig. 3e). Although the core-to-shell ratio of 8:1 produces MCs with high core fraction, the strength of their MC shell is not strong enough for handling and transportation, which is in agreement with the collapsing behavior during the SEM imaging. Therefore, it is reasonable to balance the MC strength and core fraction, and the  $M_{\text{ILSTF}}:M_{\text{ABS}}$  ratio of 4:1 was selected to prepare ILSTF MCs with a nominal strength of 55 ± 8 KPa and a core fraction of 68 ± 5 wt% for the following study.

Compared with the previous reports, this work is the first to prepare MC containing STF with a controllable size at the micrometer level. Fig. 3f and S9 illustrate that ILSTF MCs with an average diameter ranging from 260 to 66 μm are obtained by adjusting the agitation rate from 250 to 400 rpm. A higher agitation rate leads to a smaller MC diameter and narrower size distribution, which is consistent with the previous studies [5,40,41]. When the stirring speed is raised from 250 to 400 rpm, the mean core concentration of ILSTF MCs is reduced from 68 to 60 wt%, suggesting the slight influence of agitation rate on core

fraction and the high microencapsulation efficiency of this o/o emulsion solvent evaporation method. The typical ILSTF MCs prepared under the agitation speed of 250 rpm were chosen for the application investigation.

#### 2.4. Multifunctional applications of ILSTF MCs

The obtained ILSTF MCs above and the control IL MCs were respectively embedded into a PDMS matrix with a weight percentage of 30 wt%, and their energy absorption capacity was characterized by quasi-static compression and SHPB dynamic impact test. The typical compressive and impact nominal stress-strain curves are given in Fig. 4a and b and S10a. PDMS and two composites exhibit similar stress under quasi-static compression. In contrast, the stress of ILSTF MCs/PDMS rises considerably when increasing the strain rate, indicating that the shear-thickening effect of ILSTF MCs is activated upon impact. The nominal strain energies at different strain rates are obtained by integrating the stress-strain curves up to a strain of 0.2. As shown in Fig. 4c, under quasi-static loading, ILSTF MCs/PDMS has slightly more robust energy absorption capability than the IL MCs/PDMS, possibly because the viscosity and hydrostatic pressure are higher for the ILSTF core. In terms of dynamic impact, the nominal strain energy density of ILSTF MCs/PDMS is  $69.3 \pm 2.1 \text{ KJ/m}^3$  at a strain rate of  $500 \text{ s}^{-1}$ , achieving 33 % and 67 % enhancements of energy absorption ability compared with PDMS ( $52.1 \pm 1.5 \text{ KJ/m}^3$ ) and IL MCs/PDMS ( $41.6 \pm 3.4 \text{ KJ/m}^3$ ), respectively. Although the nominal strain energies of both composites increase with the rise of loading velocity due to the strain rate sensitivity of the polymer matrix [42], it is notable that the increase of energy absorption for ILSTF MCs/PDMS is more significant than that of the PDMS and IL MCs-filled sample due to the shear thickening of the ILSTF

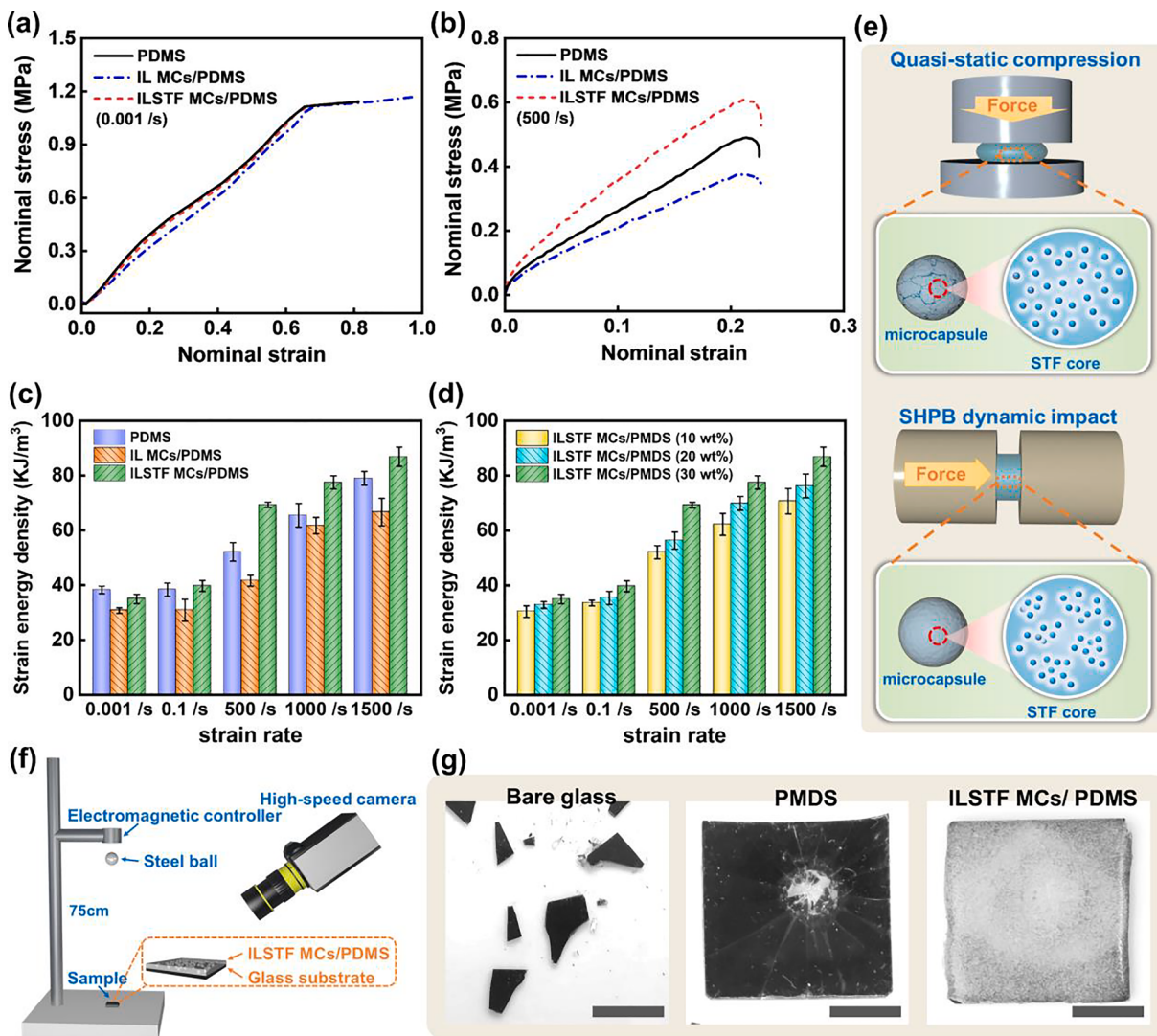


**Fig. 4.** Typical nominal stress–strain curves of PDMS and composites modified with 30 wt% IL MCs and ILSTF MCs under (a) quasi-static compression at a strain rate of 0.001 s<sup>-1</sup> and (b) dynamic impact at a strain rate of 500 s<sup>-1</sup>. (c) The nominal strain energy density of PDMS and composites modified with 30 wt% IL MCs and ILSTF MCs at different strain rates. (d) The nominal strain energy density of ILSTF MCs/PDMS with different weight percentages at different strain rates. (e) Schematic illustration of energy absorption for ILSTF MCs/PDMS under quasi-static compression and dynamic impact. (f) Schematic illustration of the ball drop testing setup. (g) Photographs of pure glass, PDMS-coated glass, and ILSTF MCs/PDMS-coated glass immediately after the collision. The scale bar indicates 10 mm.

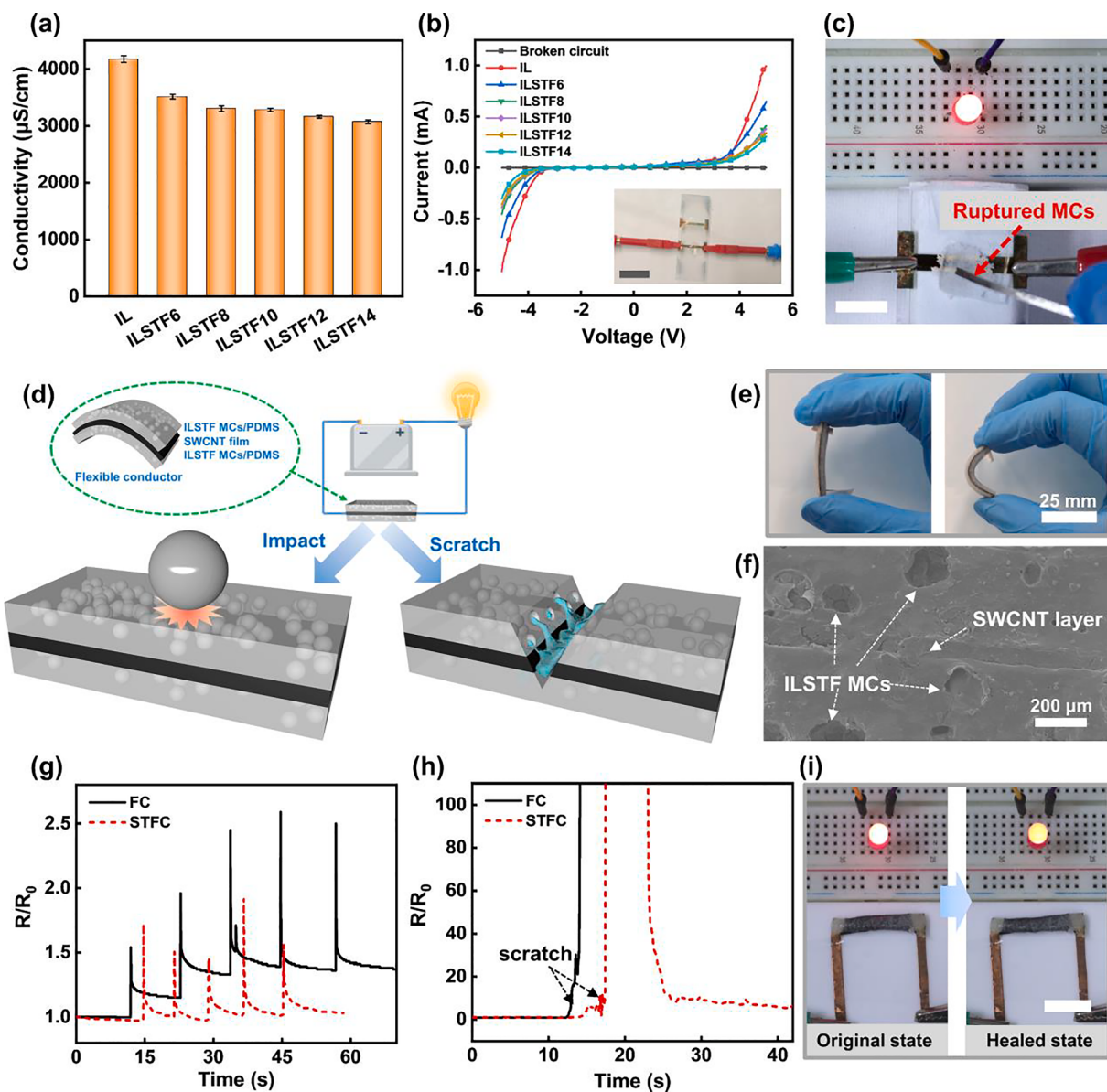
core under the impact. The influence of the weight percentage of ILSTF MCs in the matrix was further investigated. Fig. 4d shows that incorporating a higher concentration of ILSTF MCs into the matrix brings higher strain energy due to a stronger shear-thickening effect.

Fig. 4e illustrates a schematic of energy absorption of ILSTF MCs/PDMS. When it is subjected to quasi-static compression, the shear rate is too low to activate the thickening effect of the ILSTF core. The liquid phase dominates in the core, and the fracture of MC occurs under quasi-static loading. However, when the corresponding shear rate under dynamic impact is higher than the critical shear rate of the ILSTF core, the shear thickening is achieved because of the hydro-cluster formation inside the core. This shear-thickening behavior greatly strengthens the ILSTF MCs, which enables them to keep non-deforming during the impact testing and thus improves the impact resistance of composites. Therefore, it suggests that the ILSTF MCs can serve as a satisfactory energy-absorption agent for impact-resistant applications.

To further demonstrate the energy-absorption capability of ILSTF MCs/PDMS upon impact, ball drop testing was performed on a pure glass and glass coated with PDMS and ILSTF MCs/PDMS, respectively. A steel ball falls freely on the samples, and the collision process is recorded

by a high-speed camera (Fig. 4f). As shown in Fig. 4g, the bare glass and PDMS-covered glass are easily fractured, while no damage is observed for the glass coated with ILSTF MCs/PDMS, indicating that ILSTF MCs provided self-adaptive protection for substrate upon impact (Video S1-S3).

To investigate the electrochemical application of the ILSTF MCs, the conductivities of IL and ILSTFs were measured using a conductivity meter. As presented in Fig. 5a, the conductivities of pure IL and the typical ILSTF (ILSTF10) in this work reach  $4170 \pm 60$  and  $3070 \pm 34$   $\mu\text{S}/\text{cm}$ , respectively. The conductivity decreases slightly when increasing the ratio of silica because the movement of ions is restricted by the rising viscosity of ILSTF. In contrast to traditional STFs, such as PEGSTFs (Fig. S11), the conductivity of ILSTF is higher than the PEGSTF by three orders of magnitude, which extends the application fields of the ILSTF MCs. Fig. 5b shows the I-V responses of IL and ILSTFs performed on a broken electrical circuit comprised of a gold line with a 30  $\mu\text{m}$  gap. The samples show linear and stable current response until the applied voltage reaches around 3.5 V. After that, the measured current increases steeply due to the decomposition of IL [43]. The same measurement is conducted for the ruptured ILSTF MCs on the gap of the gold line



**Fig. 5.** (a) Conductivity and (b) I-V measurement for pure IL and ILSTFs. Inset is the photo of ILSTF liquid on the gap of the gold line. The black scale bar indicates 25 mm in the inset. (c) Photograph of the conductivity restoration after crushing ILSTF MCs onto the gap of the circuit. The scale bar indicates 20 mm. (d) Schematic illustration of the STFC-consisted circuit upon impact or scratch. (e) Photographs and (f) cross-sectional SEM image of the STFC. Resistance variation of the STFC-contained circuit and the control sample upon (g) impact and (h) scratch. (i) Photographs of the LED light in the original state and self-healed state after cutting. The scale bar indicates 15 mm.

(Fig. S12). The obtained I-V data is similar to that of pure IL and ILSTF, implying their potential for restoration of conductivity. To visually illustrate the conductivity-restoration functionality of ILSTF MCs, a (light-emitting diode) LED bulb is connected to the broken circuit. As expected, the LED lit up as soon as the ILSTF MCs are crushed on the gap (Fig. 5c and Video S4).

A flexible circuit with electrical stability and self-repairing is a critical part of deformable electronics. As a demonstration, we prepared a novel sandwich-like shear-thickening flexible conductor (STFC) consisting of a single-wall carbon nanotube (SWCNT) conductive film and two layers of ILSTF MCs-embedded PDMS (Fig. 5d). Fig. 5e exhibits that the STFC is free-standing and highly flexible. The cross-section SEM image of the STFC in Fig. 5f clearly shows the respective layers of SWCNTs and ILSTF MCs/PDMS. Fig. 5d displays a schematic of a simple circuit containing the STFC and a LED connected to the SWCNT layer. To investigate the impact resistance of the flexible circuit, a steel ball falls freely on the STFC, and its electrical performance is evaluated by the

ratio of instant resistance ( $R$ ) to initial resistance ( $R_0$ ). As shown in Fig. 5g, the average resistance variation ( $R/R_0$ ) of five ball-drop tests for the STFC is  $1.6 \pm 0.2$ , which is much more stable than the control specimen without ILSTF MCs (the average  $R/R_0$  is  $2.2 \pm 0.4$ ), reflecting the impact-energy-absorption ability of ILSTF MCs. Furthermore, when the FC is scratched by a razor blade, its  $R/R_0$  increases dramatically, and the circuit is broken without recovery (Fig. 5h). On the contrary, the  $R/R_0$  of the STFC-contained circuit recovers after about 10 s due to the outflow of ILSTF from ruptured MCs and reconnection of the damaged site. Fig. 5i and Video S5 show the circuit retains its conductivity after scratching the STFC, enabling the operation of the LED bulb. Based on these results, ILSTF MCs are expected to serve as a self-adaptable multifunctional agent not only for impact-resistant applications, but also for electrochemical applications such as autonomic conductivity restoration.

### 3. Conclusion

In summary, direct and scalable microencapsulation of a multi-functional ILSTF via rheological response transition by an o/o emulsion solvent-evaporation method is proposed for the first time. Taking advantage of the mechanism of solvent-evaporation microencapsulation, the high viscous ILSTF is diluted with a sufficient volume of co-solvent, which eliminates the shear-thickening effect in the meantime. This diluted solution of ILSTF can easily produce emulsion compared with neat ILSTF. Furthermore, with the evaporation of co-solvent and phase separation of the polymer shell, the ILSTF solution returns to the original ILSTF as the liquid core of MCs. This approach enables the preparation of ILSTF MCs with a controllable size at a micrometer level and extremely high thermal stability. The obtained ILSTF MCs are robust enough to be incorporated into a PDMS matrix, which displays significant improvement on impact-resistance of 33 % and 67 % increase in energy absorption capability compared with pure PDMS and the IL MCs/PDMS, respectively. Moreover, the self-adaptive STFC-contained circuit shows electrical stability under impact and autonomic conductivity restoration after damage, indicating the great potential of multifunctional ILSTF MCs for application in flexible circuits.

### Declaration of Competing Interest

The authors declare that they have no known competing financial interests or personal relationships that could have appeared to influence the work reported in this paper.

### Data availability

Data will be made available on request.

### Acknowledgement

The work was financially supported by the NSFC/RGC Joint Research Scheme of Hong Kong (Grant#: N\_HKUST 631/18, 51861165103), Foundation of Guangdong Provincial Key Laboratory of Functional Substances in Medicinal Edible Resources and Healthcare Products (No. GPKLFSHP20210), the Project of Hetao Shenzhen-Hong Kong Science and Technology Innovation Cooperation Zone (HZB-KCZYB-2020083), and the Induction of Entrepreneurship Talents Program funded by Foshan-HKUST Projects (Grant #: FSUST20-ETP06). The authors are grateful to Mark Ellwood from MAE of HKUST for the constructive discussion and input for this article.

### Appendix A. Supplementary data

Supplementary data to this article can be found online at <https://doi.org/10.1016/j.cej.2022.140819>.

### References

- [1] P. Christen, K. Ito, R. Ellouz, S. Boutroy, E. Sornay-Rendu, R.D. Chapurlat, B. Van Rietbergen, Bone remodelling in humans is load-driven but not lazy, *Nat. Commun.* 5 (1) (2014) 1–5, <https://doi.org/10.1038/ncomms5855>.
- [2] E.A. Zimmermann, B. Gludovatz, E. Schlaible, N.K. Dave, W. Yang, M.A. Meyers, R.O. Ritchie, Mechanical adaptability of the Bouligand-type structure in natural dermal armour, *Nat. Commun.* 4 (1) (2013) 1–7, <https://doi.org/10.1038/ncomms3634>.
- [3] L. Montero de Espinosa, W. Meesorn, D. Moatsou, C. Weder, Bioinspired polymer systems with stimuli-responsive mechanical properties, *Chem. Rev.* 117 (20) (2017) 12851–12892, <https://doi.org/10.1021/acs.chemrev.7b00168>.
- [4] J.F. Patrick, M.J. Robb, N.R. Sottos, J.S. Moore, S.R. White, Polymers with autonomous life-cycle control, *Nature* 540 (7633) (2016) 363–370, <https://doi.org/10.1038/nature21002>.
- [5] S. Chen, T. Han, Y. Zhao, W. Luo, Z. Zhang, H. Su, B.Z. Tang, J. Yang, A facile strategy to prepare smart coatings with autonomous self-healing and self-reporting functions, *ACS Appl. Mater. Interfaces* 12 (4) (2019) 4870–4877, <https://doi.org/10.1021/acsami.9b18919>.
- [6] Y. Zhu, M. Liu, M. Chen, L. Wu, Synthesis of blue light-responsive microspheres for autonomous self-healing coatings, *Chem. Eng. J.* 450 (2022) 138306, <https://doi.org/10.1016/j.cej.2022.138306>.
- [7] L. Ma, C. Ren, J. Wang, T. Liu, H. Yang, Y. Wang, Y. Huang, D. Zhang, Self-reporting coatings for autonomous detection of coating damage and metal corrosion: a review, *Chem. Eng. J.* 421 (2021) 127854, <https://doi.org/10.1016/j.cej.2020.127854>.
- [8] S. Chen, T. Han, J. Liu, X. Liang, J. Yang, B.Z. Tang, Visualization and monitoring of dynamic damaging-healing processes of polymers by using AI/Eigen-loaded multifunctional microcapsules, *J. Mater. Chem. A* 10 (29) (2022) 15438–15448, <https://doi.org/10.1039/d2ta02918a>.
- [9] F. Paulo, L. Santos, Design of experiments for microencapsulation applications: a review, *Mater. Sci. Eng.: C* 77 (2017) 1327–1340, <https://doi.org/10.1016/j.msec.2017.03.219>.
- [10] J.F. Morris, Shear thickening of concentrated suspensions: recent developments and relation to other phenomena, *Annu. Rev. Fluid. Mech.* 52 (2020) 121–144, <https://doi.org/10.1146/annurev-fluid-010816-060128>.
- [11] Y. Wu, W. Wang, J. Zhang, M. Sang, Y. Xu, J. Zhou, S. Wang, Y. Cai, S. Xuan, X. Gong, Liquid or solid? a biologically inspired concentrated suspension for protective coating, *Chem. Eng. J.* 428 (2022) 131793, <https://doi.org/10.1016/j.cej.2021.131793>.
- [12] S. Gürgen, M.C. Kuşhan, W. Li, Shear thickening fluids in protective applications: a review, *Prog. Polym. Sci.* 75 (2017) 48–72, <https://doi.org/10.1016/j.progpolymsci.2017.07.003>.
- [13] K. Ueno, S. Imaizumi, K. Hata, M. Watanabe, Colloidal interaction in ionic liquids: effects of ionic structures and surface chemistry on rheology of silica colloidal dispersions, *Langmuir* 25 (2) (2009) 825–831, <https://doi.org/10.1021/la803124m>.
- [14] J. Gao, R.S. Ndong, M.B. Shiflett, N.J. Wagner, Creating nanoparticle stability in ionic liquid [C4mim][BF4] by inducing solvation layering, *ACS Nano* 9 (3) (2015) 3243–3253, <https://doi.org/10.1021/acsnano.5b00354>.
- [15] J. Qin, G. Zhang, X. Shi, M. Tao, Study of a shear thickening fluid: the dispersions of silica nanoparticles in 1-butyl-3-methylimidazolium tetrafluoroborate, *J. Nanopart. Res.* 17 (8) (2015) 1–13, <https://doi.org/10.1007/s11051-015-3144-9>.
- [16] J. Qin, B. Guo, L. Zhang, T. Wang, G. Zhang, X. Shi, Soft armor materials constructed with Kevlar fabric and a novel shear thickening fluid, *Compos. B: Eng.* 183 (2020), 107686, <https://doi.org/10.1016/j.compositesb.2019.107686>.
- [17] M. Marium, M. Hoque, M.S. Miran, M.L. Thomas, I. Kawamura, K. Ueno, K. Dokko, M. Watanabe, Rheological and Ionic Transport Properties of Nanocomposite Electrolytes Based on Protic Ionic Liquids and Silica Nanoparticles, *Langmuir* 36 (1) (2020) 148–158, <https://doi.org/10.1021/acs.langmuir.9b02848>.
- [18] Y.S. Lee, E.D. Wetzel, N.J. Wagner, The ballistic impact characteristics of Kevlar® woven fabrics impregnated with a colloidal shear thickening fluid, *J. Mater. Sci.* 38 (13) (2003) 2825–2833, <https://doi.org/10.1023/A:1024424200221>.
- [19] J.N. Fowler, A.A. Pallanta, C.B. Swanik, N.J. Wagner, The Use of Shear Thickening Nanocomposites in Impact Resistant Materials, *J. Biomech. Eng.* 137 (5) (2015), <https://doi.org/10.1115/1.4029982>.
- [20] M.J. Decker, C.J. Halbach, C.H. Nam, N.J. Wagner, E.D. Wetzel, Stab resistance of shear thickening fluid (STF)-treated fabrics, *Compos. Sci. Technol.* 67 (3–4) (2007) 565–578, <https://doi.org/10.1016/j.compscitech.2006.08.007>.
- [21] M. Soutrenon, V. Michaud, Impact properties of shear thickening fluid impregnated foams, *Smart. Mater. Struct.* 23 (3) (2014), 035022, <https://doi.org/10.1088/0964-1726/23/3/035022>.
- [22] X. Zhang, W. Li, X. Gong, The rheology of shear thickening fluid (STF) and the dynamic performance of an STF-filled damper, *Smart. Mater. Struct.* 17 (3) (2008), 035027, <https://doi.org/10.1088/0964-1726/17/3/035027>.
- [23] R. Borella, R. Barry, T. Allgeuer, H. Den Hartog, Plastic hollow fibre containing a shear thickening fluid for high tensile strength fibres, *W02008115636A3* (2008).
- [24] J.G. Lundin, M.J. Bertocchi, R.B. Balow, J.H. Wynne, Polymer fibers with shear-thickening liquid cores, *US20200248338A1* (2020).
- [25] H. Zhang, X. Zhang, Q. Chen, X. Li, P. Wang, E.-H. Yang, F. Duan, X. Gong, Z. Zhang, J. Yang, Encapsulation of shear thickening fluid as an easy-to-apply impact-resistant material, *J. Mater. Chem. A* 5 (43) (2017) 22472–22479, <https://doi.org/10.1039/C7TA04904H>.
- [26] X. Zhang, H. Zhang, P. Wang, Q. Chen, X. Li, Y. Zhou, X. Gong, Z. Zhang, E.-H. Yang, J. Yang, Optimization of shear thickening fluid encapsulation technique and dynamic response of encapsulated capsules and polymeric composite, *Compos. Sci. Technol.* 170 (2019) 165–173, <https://doi.org/10.1016/j.compscitech.2018.11.040>.
- [27] X. Liu, J.-L. Huo, T.-T. Li, H.-K. Peng, J.-H. Lin, C.-W. Lou, Investigation of the shear thickening fluid encapsulation in an orifice coagulation bath, *Polymers* 11 (3) (2019) 519, <https://doi.org/10.3390/polym11030519>.
- [28] T.-T. Li, J. Huo, X. Liu, H. Wang, B.-C. Shiu, C.-W. Lou, J.-H. Lin, Characteristics, Compression, and Buffering Performance of Pomelo-Like Hierarchical Capsules Containing Shear Thickening Fluid, *Polymers* 11 (7) (2019) 1138, <https://doi.org/10.3390/polym11071138>.
- [29] S. Freitas, H.P. Merkle, B. Gander, Microencapsulation by solvent extraction/evaporation: reviewing the state of the art of microsphere preparation process technology, *J. Control. Release* 102 (2) (2005) 313–332, <https://doi.org/10.1016/j.jconrel.2004.10.015>.
- [30] J. Qin, G. Zhang, Z. Ma, J. Li, L. Zhou, X. Shi, Effects of ionic structures on shear thickening fluids composed of ionic liquids and silica nanoparticles, *Rsc Adv.* 6 (85) (2016) 81913–81923, <https://doi.org/10.1039/C6RA12460G>.

- [31] R. Hoffman, Discontinuous and dilatant viscosity behavior in concentrated suspensions. II. Theory and experimental tests, *J Colloid. Interf. Sci* 46(3) (1974) 491–506, [https://doi.org/10.1016/0021-9797\(74\)90059-9](https://doi.org/10.1016/0021-9797(74)90059-9).
- [32] H. Barnes, Shear-thickening ("Dilatancy") in suspensions of nonaggregating solid particles dispersed in Newtonian liquids, *J. Rheol.* 33 (2) (1989) 329–366, <https://doi.org/10.1122/1.550017>.
- [33] S.R. Raghavan, H.J. Walls, S.A. Khan, Rheology of silica dispersions in organic liquids: new evidence for solvation forces dictated by hydrogen bonding, *Langmuir* 16 (21) (2000) 7920–7930, <https://doi.org/10.1021/la991548q>.
- [34] S.R. Raghavan, S.A. Khan, Shear-thickening response of fumed silica suspensions under steady and oscillatory shear, *J Colloid. Interf. Sci* 185 (1) (1997) 57–67, <https://doi.org/10.1006/jcis.1996.4581>.
- [35] F. Meng, S. Wang, Y. Wang, H. Liu, X. Huo, H. Ma, Z. Ma, H. Xiong, Microencapsulation of oxalic acid via oil-in-oil (O/O) emulsion solvent evaporation, *Powder technology* 320 (2017) 405–411, <https://doi.org/10.1016/j.powtec.2017.07.073>.
- [36] A. Loxley, B. Vincent, Preparation of poly (methylmethacrylate) microcapsules with liquid cores, *J Colloid. Interf. Sci* 208 (1) (1998) 49–62, <https://doi.org/10.1006/jcis.1998.5698>.
- [37] S. Tang, M. Yourdkhani, C.M. Possanza Casey, N.R. Sottos, S.R. White, J.S. Moore, Low-ceiling-temperature polymer microcapsules with hydrophobic payloads via rapid emulsion-solvent evaporation, *ACS Appl. Mater. Interfaces* 9 (23) (2017) 20115–20123. <https://doi.org/https://doi.org/10.1021/acsmami.7b05266>.
- [38] P.J. Dowding, R. Atkin, B. Vincent, P. Bouillot, Oil core–polymer shell microcapsules prepared by internal phase separation from emulsion droplets. I. Characterization and release rates for microcapsules with polystyrene shells, *Langmuir* 20 (26) (2004) 11374–11379. <https://doi.org/https://doi.org/10.1021/la048561h>.
- [39] Y. Cao, Y. Chen, X. Sun, T. Mu, Quantification of ionic liquids concentration in water and qualification of conjugated and inductive effects of ionic liquids by UV spectroscopy, *Clean-Soil Air Water* 42 (8) (2014) 1162–1169, <https://doi.org/10.1002/clen.201300237>.
- [40] J. Yang, M.W. Keller, J.S. Moore, S.R. White, N.R. Sottos, Microencapsulation of isocyanates for self-healing polymers, *Macromolecules* 41 (24) (2008) 9650–9655, <https://doi.org/10.1021/ma801718v>.
- [41] M. Huang, J. Yang, Facile microencapsulation of HDI for self-healing anticorrosion coatings, *J. Mater. Chem. C* 1 (30) (2011) 11123–11130, <https://doi.org/10.1039/CJCM10794A>.
- [42] X. Zhang, P. Wang, D. Sun, X. Li, J. An, T. Yu, E.-H. Yang, J. Yang, Dynamic plastic deformation and failure mechanisms of individual microcapsule and its polymeric composites, *J. Mech. Phys. Solids* 139 (2020), 103933, <https://doi.org/10.1016/j.jmps.2020.103933>.
- [43] B. Yiming, X. Guo, N. Ali, N. Zhang, X. Zhang, Z. Han, Y. Lu, Z. Wu, X. Fan, Z. Jia, Ambiently and Mechanically Stable Ionogels for Soft Iontronics, *Adv. Funct. Mater.* (2021) 2102773, <https://doi.org/10.1002/adfm.202102773>.